Polymer Degradation and Stability 152 (2018) 147–161

Contents lists available at ScienceDirect

Polymer Degradation and Stability

journal homepage: www.elsevier.com/locate/polydegstab

Kinetics, evolving thermal properties, and surface ignition of carbon fiber reinforced epoxy composite during laser-induced decomposition

Nicholas C. Herr*, Ashley E. Gonzales, Glen P. Perram

Department of Engineering Physics, Air Force Institute of Technology, 2950 Hobson Way, Wright-Patterson Air Force Base, Ohio, 45433-7765, United States

ARTICLE INFO

Article history:
Received 2 February 2018
Received in revised form
15 March 2018
Accepted 5 April 2018
Available online 11 April 2018

Keywords:
Carbon fiber reinforced polymer
Fiber laser damage
Thermal imagery
Emissivity

ABSTRACT

The decomposition kinetics, heats of reaction, evolving thermal conductivity and emissivity, and surface ignition conditions of carbon fiber reinforced polymer (CFRP) composites during laser-induced polymer matrix decomposition were investigated. Woven carbon fiber-epoxy panels of different thicknesses were irradiated with a 1.07-μm, 2-kW ytterbium fiber laser at irradiances of 5–525 W/cm^2. The changing front and backside surface temperatures were measured using a mid-wave infrared camera, adjusted using measured emissivity of irradiated and un-irradiated CFRP samples. The evolving temperature maps were fit to a 3D, explicit, finite difference, thermal model to estimate Arrhenius kinetic rate parameters, heats of reaction, and thermal conductivity during a two-step epoxy decomposition reaction and a single stage char oxidation reaction. The kinetics is not strongly dependent on heating rates of 20–700 °C/sec and parameters determined at lower laser powers extrapolate well to higher powers. Surface ignition occurs at critical surface temperatures of 1198 ± 50 °C.

1. Introduction

The use of carbon fiber reinforced polymer (CFRP) is increasing in many aerospace, military, and automotive applications [1]. Thermal damage and combustion has been studied and modeled primarily for fire science applications [2–4], at lower heating rates and often for piloted ignition. For piloted ignition of an epoxy matrix, volatile surface fluxes of approximately 7.5 g/m^{2}s [5] are required, a condition that is produced by incident heat fluxes of at least 1.3 W/cm^2. In contrast, lasers provide many times the necessary surface heating to produce volatile products but provide no ready ignition source, producing much different ignition criteria. The fielding of tactical high-energy laser (HEL) weapon systems and the proliferation of fiber lasers makes CFRPs likely target materials in future laser engagements [6–8]. We seek to develop a model for evolving material thermal and optical properties, and decomposition kinetics capable of describing ignition and mass loss under high irradiance HEL conditions. In particular, surface temperatures and hydrocarbon plume concentrations required for ignition and characterizing the rate of mass loss at high heating rates is critical for weapons applications.

At the fiber laser wavelength of 1.07 μm, the epoxy matrix is highly transmitting and carbon fiber is highly absorbing [9], resulting in laser absorption primarily into the first fiber layer followed by conduction to the surrounding epoxy [10]. Carbon fibers are thermally robust and require high irradiance to achieve CFRP burn-through, but much less to decompose the epoxy resin. Cured epoxy softens (120 °C) and dehydrates (250–300 °C) before decomposing via random chain scission (300–450 °C) to produce volatile fragments and char [11]. Resin decomposition can have damaging effects due to fouling and combustion of volatiles on both interior and exterior panel surfaces and significant reductions in CFRP compressive strength [2].

As volatile decomposition vapors accumulate in the vicinity of the laser spot, they can be detected and their relative concentrations tracked during the period leading up to ignition using an imaging Fourier Transform Spectrometer (IFTS). IFTS uses a Michelson interferometer and a detector array to generate interference spectra at every pixel in a scene. IFTS has been previous used to analyze the constituents of industrial smokestacks [12], jet engine exhaust plumes [13], chemical plumes [14], natural gas flare emissions [15], and HEL material degradation plumes (fiberglass [16], polymethyl methacrylate (PMMA) [17], and graphite [18]).

This work uses high-speed thermal imagery and a simplified thermal model to determine evolving front and back CFRP surface temperatures and to estimate unknown thermal properties and

* Corresponding author.
E-mail address: nicholas.herr@afit.edu (N.C. Herr).

https://doi.org/10.1016/j.polymdegradstab.2018.04.007
0141-3910/

kinetic parameters throughout epoxy decomposition at low laser irradiance. Results are applied to the prediction of surface temperatures at higher laser powers. The necessary conditions for surface ignition under HEL irradiation are also determined using thermal and IFTS imagery.

2. Experimental

Commercially available CFRP panels were obtained from Protech Composites Inc. in thicknesses of 1.7, 2.4, 3.2 mm and contained 4,6, or 8 plies of 6K 2 × 2 twill weave carbon fiber fabric. The polymer matrix was a Bisphenol A diglycidyl ether (DGEBA) based epoxy resin blend and was injected under vacuum. The hardener identity was not released by the manufacturer.

Panels were irradiated by a 2-kW continuous wave IPG Photonics ytterbium doped fiber laser at 1.07 μm, as shown in Fig. 1. Front and back surface temperatures were simultaneously recorded with a mid infrared camera by placing a flat mirror behind the CFRP panels. A beam splitter was used to illuminate a stationary scatter plate and the spatial and temporal laser beam irradiance variation was recorded by near infrared (NIR) camera. A 30-Hz visible camera was used to witness each test. Tests were conducted on an open optical table with ceiling mounted ventilation hood (upward flow speed approximately 0.2 m/s).

Square, 10.38 cm × 10.38 cm, 3.2-mm thick panels were irradiated at 5, 10, 36, and 64 W/cm^2, with the square 1.7-and 2.4-mm thick panels irradiated at 10 and 36 W/cm^2. The laser spot diameter was 6 cm for all but the 64 W/cm^2 shot (2.3 cm diameter). Spot size was stable and measured at 1/e^2 of peak value. Reported irradiance values are the average irradiance within 0.5 cm of laser center. High irradiance (85–525 W/cm^2) experiments were conducted on 30.48 cm × 15.24 cm strips with a 2.4-cm diameter laser spot and 15.24 cm × 2.54 cm strips with a 1.65-cm diameter laser spot. Tests were run for two minutes or until surface ignition occurred. Irradiance reached peak levels in approximately 0.5 s and irradiance in a given pixel varied by ± 0.4–1.7% with the highest instability nearest laser hot spots.

Thermal imagery was recorded at 160 × 128 pixel resolution using a FLIR SC6000 MWIR camera. The camera was operated with a band pass filter from 3.8 to 4.0 μm and a neutral density filter of O.D. 1.0. On low irradiance tests, a silvered mirror was placed behind the sample and angled to allow the camera to view both the front and backside of the panel side-by-side in the same frame. The test panels were imaged at an angle of 32.6° off normal, in the same horizontal plane. Spatial resolution was 1.49 mm/pixel x 1.22 mm/pixel for the front side and 1.61 mm/pixel x 1.48 mm/pixel for the back.

The mid-infrared imagery was corrected for detector non-uniformity, non-linearity, bad pixels and detector spectral response on a pixel-by-pixel basis using an Electro-Optical Industries CES600-06 wide area blackbody at T = 50–600 °C. Images were collected sequentially at four integration times (0.1, 0.3, 2, and 4 ms for laser irradiance of 10 W/cm^2) at frame rates of 120–240 frames per second (30–60 fps per integration time). The multiple integration times extended the dynamic range to 300–2500 K.

The accuracy of the surface temperature is primarily dependent on surface emissivity at the 3.9-μm wavelength of the thermal camera. The spectral emissivity of undamaged and damaged CFRP material was measured from 2 to 25 μm with a SOC-100 Hemispherical Directional Reflectometer (HDR) manufactured by Surface Optics Corp at temperatures up to 500 °C [19]. Room temperature absorptivity (α) of undamaged material, charred material, and bare fibers at 1.07 μm were also measured using a Cary 5000 UV-Vis-NIR spectrophotometer. Absorptivity of undamaged CFRP was 0.93. Surface charring due to thermal decomposition increased α to 0.98 and char oxidation to bare fiber decreased α to 0.86.

Spatially- and temporally-resolved (~0.5 mm and ~10 Hz) infrared emission spectra (λ = 1.5–5 μm) of the decomposition plume prior to ignition were measured from the side using a Telops Hyper-Cam MWIR Imaging Fourier Transform Spectrometer (IFTS), as shown in Fig. 1(b) [20]. Many of the volatile epoxy decomposition products have IR absorption peaks at 3000 cm^{-1} resulting from C-H bond stretching and near 3700 cm^{-1} due to phenolic O-H stretching. The observed emission is used to monitor the relative concentration of volatiles prior to ignition. The Telops IFTS spectral resolution was 16 cm^{-1} with 128 × 64 pixel images acquired at 9–14 frames per second and a spatial resolution of 0.46 cm/pixel.

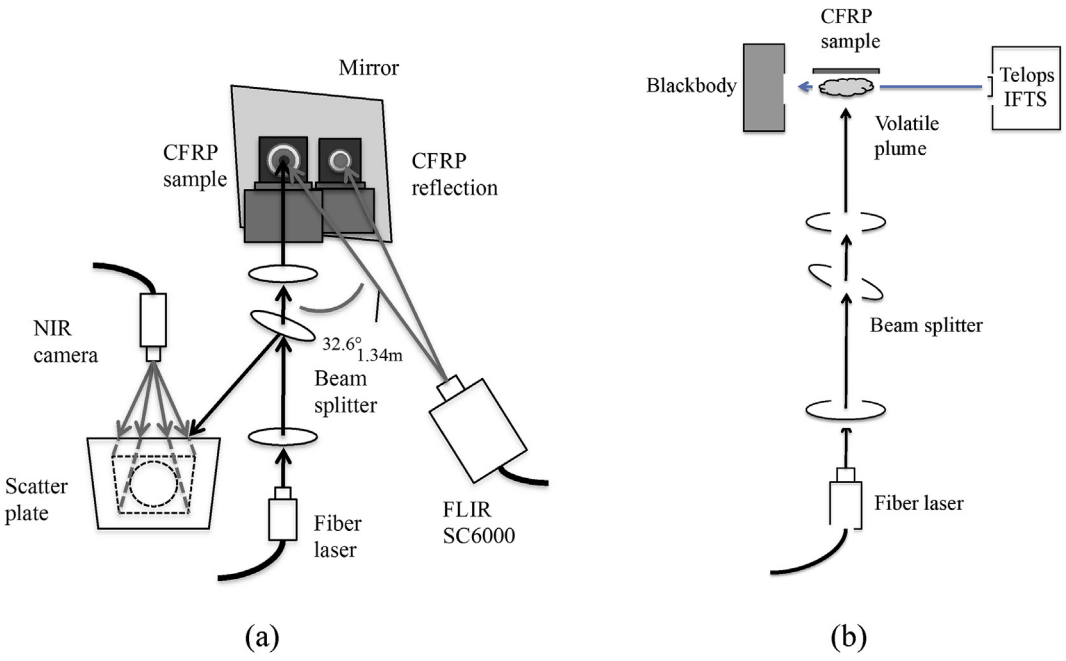

Fig. 1. Experimental Schematic for: (a) surface temperature imaging and (b) plume emission hyperspectral imaging.

3. Results

3.1. Sample response

A sequence of visible images during laser irradiation of a 3.2-mm panel at 35.7 W/cm^2 is shown in Fig. 2. Polymer decomposition produced billowing clouds of volatile products and soot beginning at a surface temperature of approximately 430 °C. Ignition (at > 20 W/cm^2) produced a large initial fireball before settling to a front surface flame corresponding to areas of removed resin. The test was terminated shortly after ignition and the laser spot cooled rapidly. The flame did not immediately extinguish, slowly diminishing as thermal volatile production decreased. Once ignited, the surface flame extended well beyond the top edge of the panel. At 35.7 W/cm^2 and 6-cm spot size, there were enough volatiles being produced on the backside of the panel to be ignited by the front side flames at surface temperatures well below those necessary for initial front side ignition (approximately 600 °C less).

The resulting CFRP panel had a concentric-ring appearance. Working outward, laser center was reduced to bare carbon fiber with no apparent fiber damage, next to a ring of porous char, then a ring of discolored resin and finally undamaged resin. The radius of visible change ranged from approximately 2–3.5 cm for 5–35.7 W/cm^2 using the 3 cm laser beam radius. Given enough laser power and time, similar trends were observed on the panel backsides as well. The top panel edges suffered additional degradation from burning volatiles. Some panels also exhibited a ring of black tar-like deposits outside the laser spot from condensing volatiles.

3.2. Mass loss

Mass loss increased with total incident laser energy with an increased rate for cases that achieved ignition and smaller laser spot size as shown in Fig. 3. No significant mass loss is observed for total incident energies E < 7.7 kJ and <5.2 kJ for non-ignition and ignition cases, respectively, at 6-cm laser spot diameter (average fluences of 290 and 195 J/cm^2). When the laser spot diameter is reduced to 2.3 cm, no mass loss is observed for E < 2.8 kJ (average fluence of 663 J/cm^2). The mass loss above this threshold increases approximately linearly with incident energy at rates of 109, 158, and 224 mg/kJ for non-ignition (6 cm) and ignition at 6-cm and 2.3-cm spot sizes, respectively. The appearance of combustion flames increases the mass loss rate by 45%.

3.3. Ignition conditions

Ignition was observed for all irradiances >21 W/cm^2 with the ignition times as shown in Fig. 4. Ignition times relative to the laser initiation were determined from both the visible witness camera and confirmed from a temperature spike present in the FLIR data.

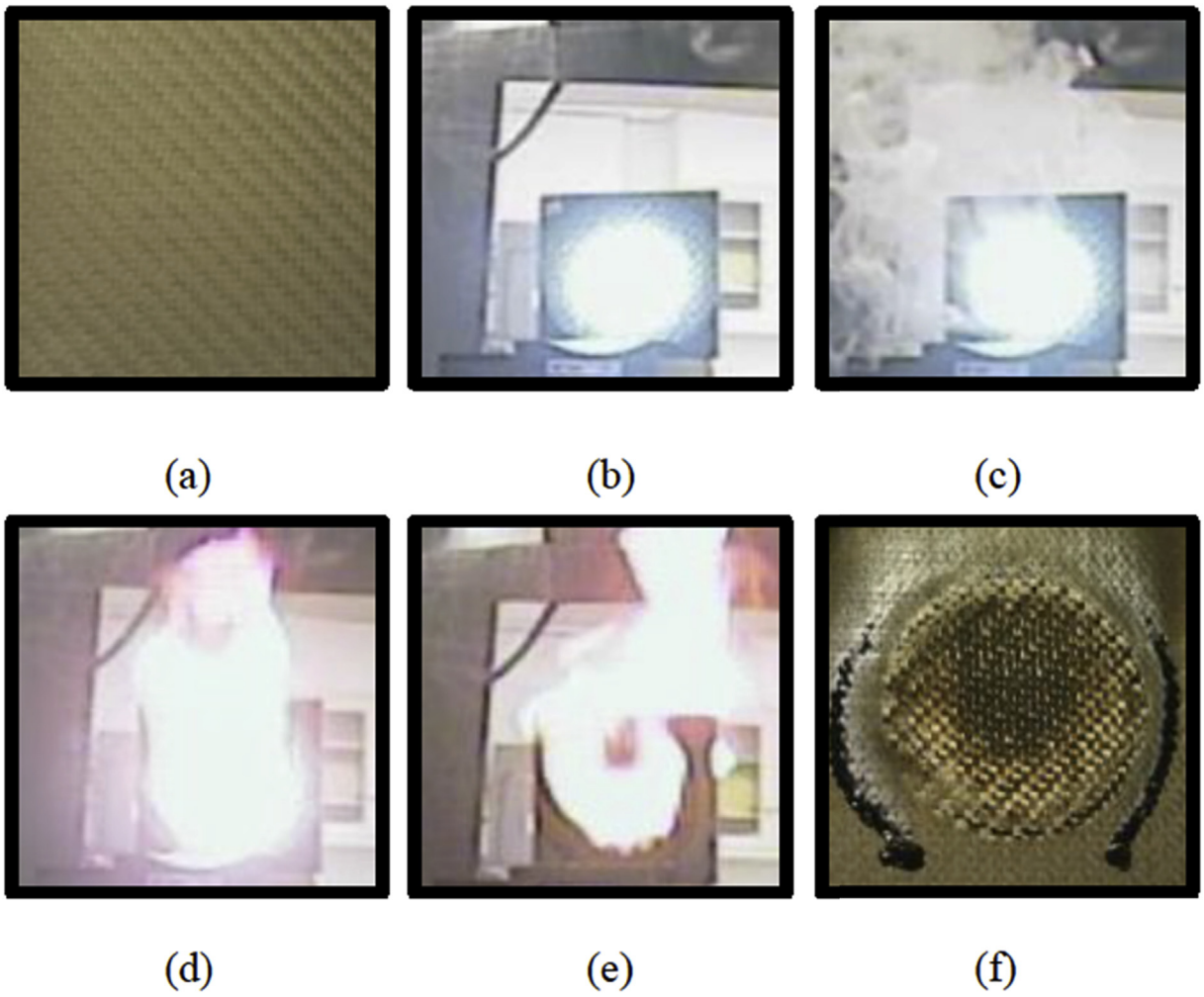

Fig. 2. Visible images of 3.2 mm panel, 35.7 W/cm^2: (a) undamaged CFRP panel, (b) laser spot (1 s), (c) smoky decomposition plume (5 s), (d) surface flame (45 s), (e) flame after laser-off (58 s), and (f) final damaged panel.

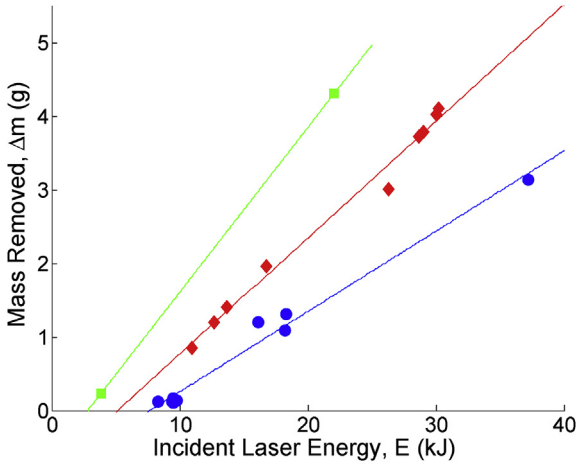

Fig. 3. Sample mass loss under (♦) ignition and (●) non-ignition conditions at 6 cm spot size, and ignition at 2.3 cm spot (■).

The witness camera and the mid IR camera were synchronized using the FLIR IRIG time code. The time when the laser was turned on was determined with an accuracy of 0.03 s from the 30 Hz visible witness camera. Most FLIR data were observed at > 120 Hz.

The threshold for ignition occurs near 21 W/cm^2 with some tests requiring higher irradiance. At 35 W/cm^2, ignition regularly occurs at 40–50 s. As irradiance increases, ignition times decrease rapidly to 2.1 s by 100 W/cm^2 and 0.07 s at 525 W/cm^2, near the measurement limit in this work. Ignition times show a small dependence on sample thickness, decreasing from an average of 43.6 s to 28.4 s to 24.1 s as thickness decreases from 3.2 mm to 2.4 mm to 1.7 mm, at 35 ± 2 W/cm^2.

Ignition depends on a minimum concentration of fuel in the form of polymer matrix decomposition products and an ignition source. In the case of piloted ignition, as in a fire scenario, a ready ignition source is ever present and ignition occurs at a mass loss rate of 0.0075 kg/m^{2}s (the necessary condition) and is achieved at surface heat fluxes as low as 2.5 W/cm^2 [12]. Results presented here indicate that laser heated polymer matrix composites require surface heat fluxes on the order of 10 times higher before ignition occurs.

The concentration of flammable polymer decomposition products near the surface was determined from hyperspectral imagery. A broadband mid IR image of the emissive plume observed with the IFTS spectrometer is shown in Fig. 5(a). The laser is incident from the left and the carbon fiber sample is positioned vertically with front surface and laser center at (x, y) = (0, 0). The turbulent smoky plume, hot region at laser center, cool edge of the sample in profile from y = 0–3 mm, and backside heating can be clearly seen. The mid IR spectrum at each pixel along the center of the laser spot, traversing the plume from far in front of the panel to behind the panel (each labeled in part(a)), is provided in Fig. 5(b). Several pixels passing directly through the most intense region in the broadband image display molecular features from 2677 to 3201 cm^{-1} and a sharper peak from 3600 to 3700 cm^{-1}. An additional peak that appears to be correlated with these peaks appears at 1959-2337 cm^{-1}.

Many of the decomposition products resulting from decomposition of the epoxy matrix in CFRP have been identified [21] and have characteristic absorption peaks centered near 3000 cm^{-1} due to C-H bond stretching and at 3700 cm^{-1} due to phenolic O-H bond stretching. However, their production ratios are not well known and their absorption cross-sections are unavailable. This limits the tracking of decomposition products in the plume to relative concentrations estimated from the changing peak areas.

Peak areas are calculated as illustrated in Fig. 6. After smoothing using a moving average filter with a span of 5 points, the data in four spectral regions lacking strong features (shown in blue) is fit to a second-order polynomial and used to remove the blackbody baseline to isolate the peak areas only. Then the peak areas in the three spectral regions of interest (1959-2337 cm^{-1}, 2677-3201 cm^{-1}, and 3600-3700 cm^{-1}) are numerically integrated. This procedure is repeated for every pixel in each frame to produce images of changing volatile peak areas as a function of spatial location and time throughout each test. The feature near 5000 cm^{-1} is an artifact of calibration, which is poor above 4000 cm^{-1}.

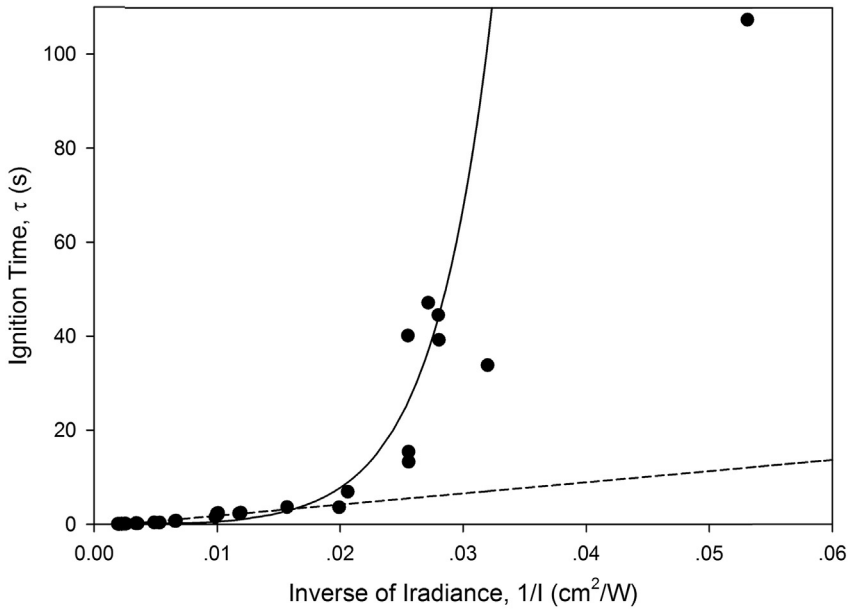

Fig. 4. Ignition times as a function of laser irradiance with curve fits to: (—) Eq (1) and (□) Eq (2).

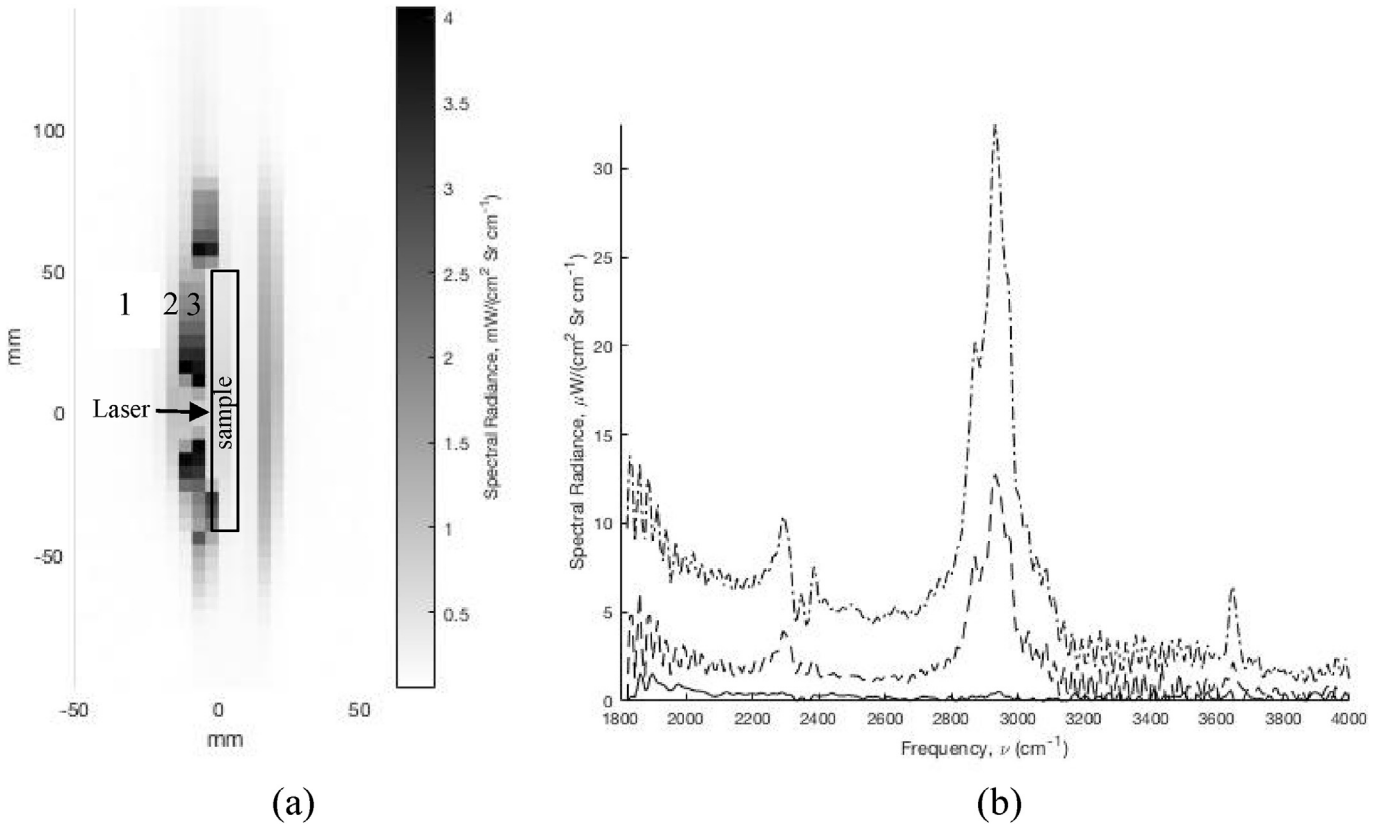

Fig. 5. (a) MWIR IFTS broadband image with the sample in profile (5 W/cm^2 laser coming from the left) and (b) FTIR spectra at multiple pixels in a row above laser center, from far in front of the sample (— at position 1 in (a)), to the edges of the plume (– at 2), to the center of plume (-·- at 3).

The pixel with maximum peak area for each spectral band in each frame near laser center is plotted in Fig. 7. The relative concentrations quickly rise from zero and establish a steady concentration several seconds after the laser is turned on. The three peak areas are linearly correlated with one another, suggesting a single-step volatile-producing decomposition reaction. This concentration is relatively unchanged for the remainder of the laser shot until ignition occurs. At this point, the plume becomes optically thick and the IFTS detector saturates from the intensity of the sooty combustion flame.

Surface temperatures at ignition were determined from the thermal imagery at laser center in the frame immediately before ignition. Temperatures at laser center are shown in Fig. 8 as a function of laser intensity. Surface temperature at ignition does not appear to be dependent on laser intensity or surface heating rate. Ignition temperatures are approximately normally distributed around 1198 °C with a standard deviation of 50 °C for all laser intensities, sample sizes, and laser spot diameters tested.

These ignition temperatures and previous volatile concentrations are not consistent with a required minimum concentration of volatile products near the surface for ignition to occur as in piloted ignition. Instead, sufficient volatiles are present and waiting for the surface temperatures to reach the critical surface temperature (1198 ± 50 °C) to cause ignition. One exception to this occurs in cases where front side ignition occurs quickly and flames reach beyond the top of the sample. In this case of piloted ignition, backside volatiles are present in suitable quantities to be externally ignited at much lower surface temperatures (approximately 700 °C).

Thus, the ignition times shown in Fig. 4 are dependent on reaching a critical surface temperature and can be modeled by accurately predicting the time to reach the ignition temperature. For the simple case of laser melting of a thin metal plate, the time required to reach the melt temperature, τ_m, can be predicted by a 1-D longitudinal thermal diffusion model:

$$\tau_m = \frac{F_m}{I} + \tau_l \tag{1}$$

where the melt fluence, F_m, is determined by the enthalpy required to melt, and the longitudinal diffusion time, τ_l, is determined by the sample thickness [22]. A linear fit of Eq (1) is shown in Fig. 4 for irradiance, I > 50 W/cm^2, yielding $F_m = 237 \pm 10$ J/cm^2. This fluence is considerably less than the value predicted to raise the sample temperature to the ignition temperature, ~450 J/cm^2, using the material properties in Table 1.

The upward curvature in Fig. 4 might be caused by 2D radial diffusion effects, as described in Ref. [22]:

$$\left(\frac{F_m}{\tau_r}\right)\left(\frac{1}{\alpha I}\right) = ln\left(\frac{\tau_m}{1.78\tau_r}\right) + \frac{2\tau_r}{\tau_m} ln\left(\frac{\tau_m}{1.78\tau_r}\right) + \frac{2\tau_r}{\tau_m} \tag{2}$$

where τ_r is the radial diffusion time. A fit to Eq (2) is also provided in Fig. 4, excluding the one very low irradiance point, yielding a melt fluence of $F_m = 17 \pm 2$ J/cm^2 and radial diffusion time of 76 ± 9 ms. The radial diffusion time is much less than would be expected from the laser spot size and material properties in Table 1 (~60 s) and the fluence would imply a much smaller temperature rise than the ignition temperature. Explaining our results on the basis of radial diffusion would require a diffusivity much greater (~1000×) than that of CFRP. These results are not surprising, as the kinetics are quite different than those encountered for a laser

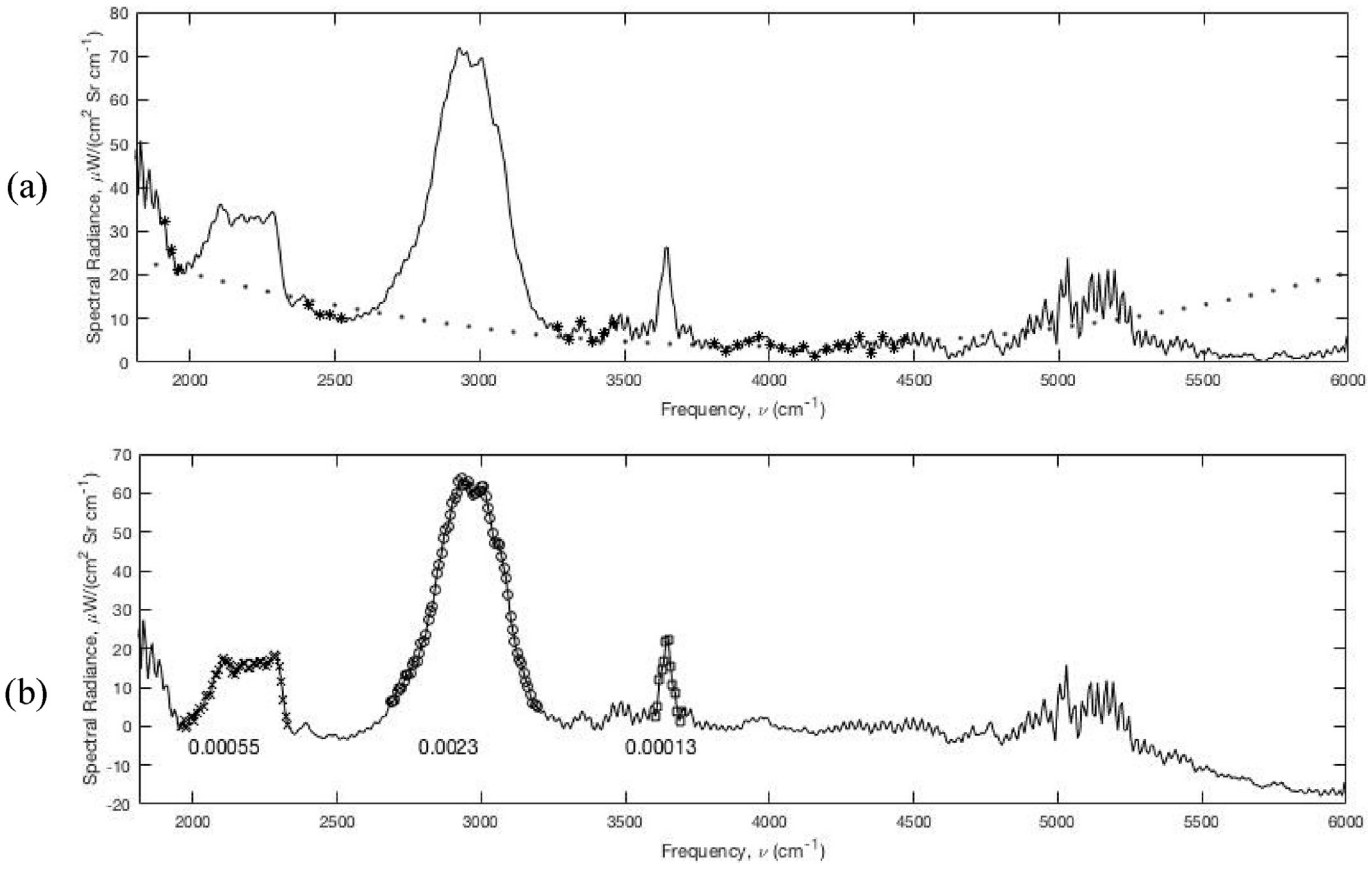

Fig. 6. Illustration of peak area calculation. Smoothed calibrated spectra (—) in (a) are fit to a 2nd order polynomial (in regions marked with *) to remove the baseline. Peak areas (b) are then numerically integrated to produce the relative concentrations over time shown in Fig. 7.

weapon penetrating a metal casing. For CFRP, energy is lost due to endothermic polymer decomposition reactions rather than radial diffusion, thermal properties change dramatically during decomposition, and volatile organics are produced at much lower temperatures than the ignition temperature. These effects must be included to accurately model the temperature distribution and predict the ignition temperature and time.

3.4. Surface emissivity

To extract surface temperature from the IR imagery, the evolving surface emissivity is required. The emissivity of the CFRP samples was studied using the SOC-100 hemispherical directional reflectometer (HDR). The wavelength and temperature dependence of the emissivity for undamaged and damaged samples is provided in Fig. 9. The emissivity of the undamaged CFRP samples is high and largely independent of wavelength, and gray body approximation would be appropriate. However, as the surface chars and exposes bare fibers, the emissivity declines and exhibits a stronger wavelength dependence. The temperature dependence of the emissivity at the 3.9 μm band pass for the infrared camera is illustrated in Fig. 9(b). The undamaged CFRP samples were measured from room temperature up to a maximum of 125 °C to avoid decomposing the resin. A larger decrease in emissivity occurs during phase changes, with smaller reductions within a given phase.

The emissivity data was combined to yield a single temperature-dependent emissivity curve at 3.9 μm, taking into account CFRP phase transitions at characteristic temperatures and distinct transition points in this testing. For all temperatures below 300 °C, $\varepsilon = 0.93$, reflective of undamaged CFRP. From 300 to 400 °C, emissivity decreases from $\varepsilon = 0.93$ to 0.86 linearly with temperature to simulate decreasing emissivity as the resin decomposes. From 400 to 500 °C, emissivity is held constant at 0.86 but decreases further to 0.77 from 500 to 600 °C as the char is oxidized to leave bare carbon fiber. From 600 °C onward emissivity decreases with temperature according to $\varepsilon = 0.792 - 0.06$ (T/1000 K).

The sensitivity of temperature determination to emissivity at 3.9 μm can produce systematic errors of up to 100 C. For $\varepsilon = 0.75 \pm 0.1$ the error in IR imagery temperatures ranges from 500 ± 25 C to 1400 ± 125 C [23]. The statistical error is defined by detector noise and is much lower, typically 2–3 °C.

3.5. Surface temperatures

Laser irradiance and surface temperature profiles for a 3.2 mm CFRP sample are provided in Fig. 10. The laser spot at 9.9 W as imaged at the scatter plate in Fig. 10(a) is non-Gaussian with two major hot spots near beam center. The laser spot diameter was 6 cm ($1/e^2$). The infrared imagery and surface temperatures at multiple integration times along a vertical, central slice is illustrated in Fig. 10(b) and (c). At longer integration times (2 and 4 ms) pixel saturation occurs near laser center. At shorter integration times (0.1 and 0.3 ms) cool pixels near the sample edge are indistinguishable from the background signal. Calibrating surface temperatures at each integration time separately and merging them together yields a complete surface temperature map. Pixels of very low signal or saturation were ignored and multiple good temperature readings were averaged (difference ranged from 2 to 12 °C). The full

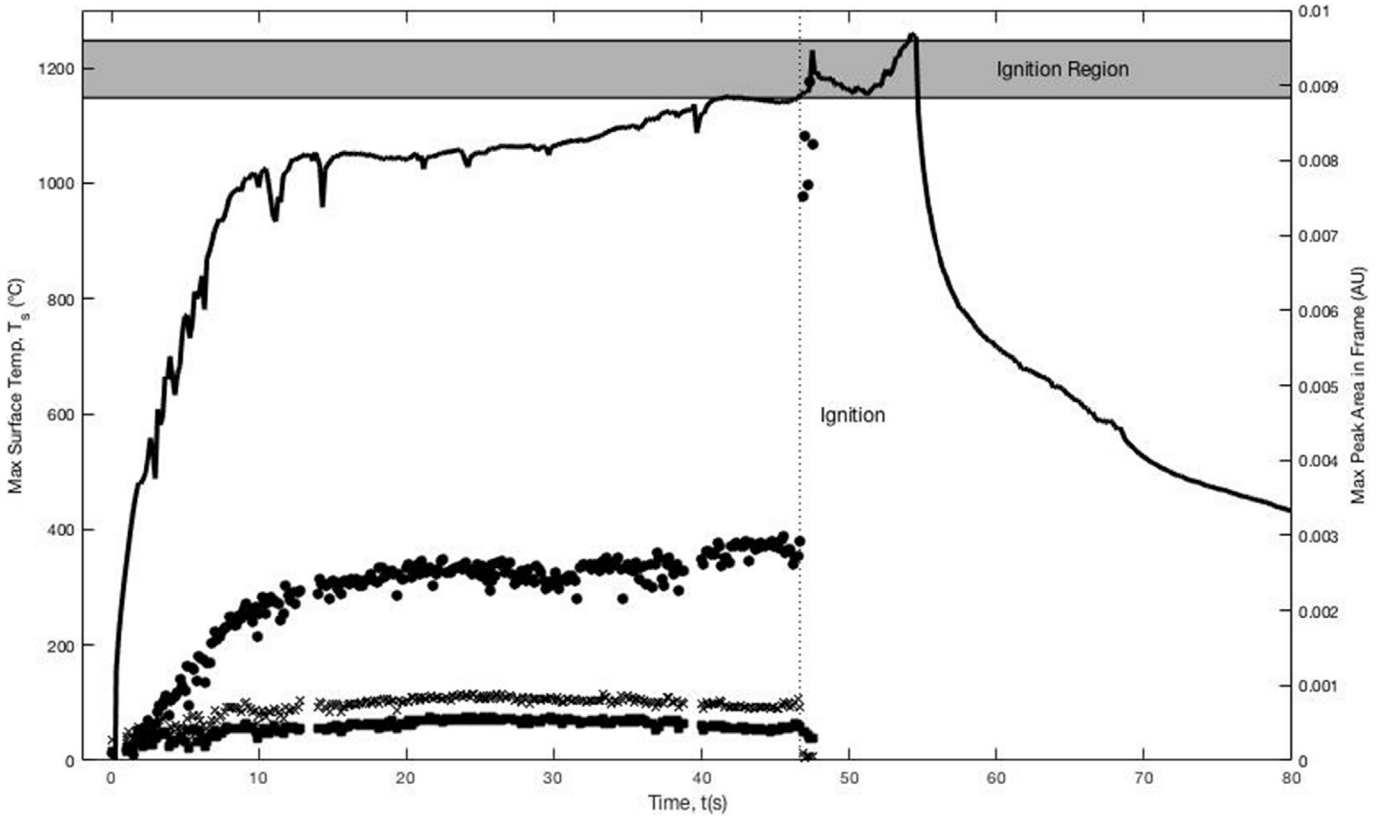

Fig. 7. Maximum volatile peak areas and surface temperatures (T_s) at 37 W/cm^2. Peak areas from 2677 to 3201 cm^{-1} are greatest (•), followed by peak areas from 1959 to 2337 cm^{-1} (x), and peak areas from 3600 to 3700 cm^{-1} (■).

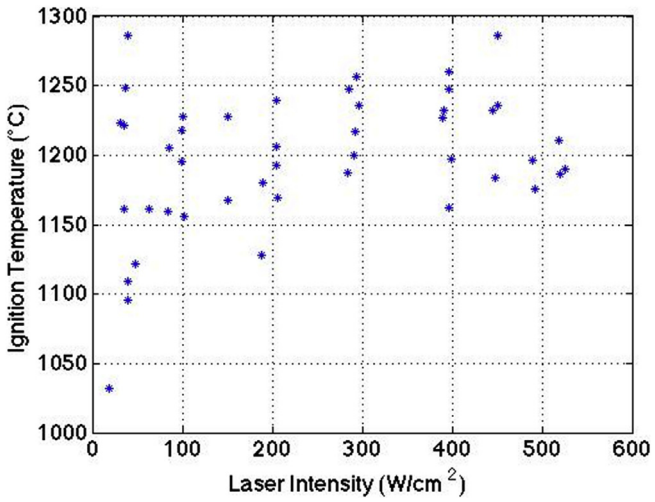

Fig. 8. Ignition temperatures as a function of laser intensity.

calibrated ($\varepsilon = 0.85$) front surface temperature map at 10 W/cm^2 and 30 s is provided in Fig. 10(d). A slight camera misalignment produced an internal reflection of approximately 1% that displaces laser center 34 mm to the right and 22 mm upward (temperatures from this region are not used). The surface temperature distribution is generally radially symmetric and mirrors the laser input with broadening due to thermal diffusion. The impact of convection on relative temperatures above and below the laser spot is minimal.

Fig. 11(a) compares the evolution of the front and backside temperatures of 3.2 mm thick samples at laser center for several laser irradiances. Irradiances of 5–64 W/cm^2 produced steady-state surface temperatures of 500–1300 °C, initial heating rates of 10–330 °C/s, and final backside temperatures of 180–450 °C.

At 5 W/cm^2, several distinct temperature regions are observed: (1) initial heating of undamaged material (0–26 s, 27–260 °C), (2) start of decomposition (dehydration) producing increased heating rate (26–32 s, 260–400 °C), (3) peak decomposition with momentary cooling (32–41 s, 400–430 °C) and (4) gradual heating for remainder of test (41–120 s, 400–550 °C). At 9.9 W/cm^2, a similar behavior was exhibited, only at a faster rate and a higher steady-state temperature (T = 780 °C) was reached. At 35.7 W/cm^2, surface decomposition occurs rapidly and the surface reaches a momentary steady state condition by 10 s and T = 1020 °C before resuming heating leading to ignition. Finally, At 63.7 W/cm^2, initial heating is very rapid and surface temperatures reach 1400 °C. Backside temperatures show a steep initial increase but level off around 175 °C momentarily for all irradiance levels. Increasing irradiance shortens this interval, followed by heating to higher temperatures. Rapid cool down is observed when the laser is turned off for all samples with the front side cooling more rapidly than the backside of the panel, leading to a crossover point with a temperature differential that increases with irradiance.

Fig. 12 compares the temperature profiles for decreasing sample thicknesses at a constant 9.9 W/cm^2 irradiance. As sample thickness decreases, front side steady state temperatures increase modestly. Backside temperatures show a similar progression, reaching an irradiance-dependent steady state temperature more quickly as irradiance is increased. Thinner samples display little temperature gradient during sample cool-down. Radial temperature distribution at 60 and 120 s are shown in Fig. 13 for 5 W/cm^2 and 9.9 W/cm^2.

Table 1
Thermal parameters derived in this work compared with prior studies.

Parameter	[26][a]	[27]	[24][d]	This work
Resin density (g/cm^3)	–	0.9	–	1.1
Fiber density (g/cm^3)	–	1.76	–	1.76
Composite density (g/cm^3)	–	–	1.81	1.463
Fiber fraction (w/w)	0.5	–	.605	0.55
k_{xy} res (W/m K)	–	–	–	5
k_{xy} dry (W/m K)	–	–	–	5
k_{xy} char (W/m K)	–	–	–	3
k_{xy} fib (W/m K)	–	–	–	3
k_z res (W/m K)	0.162	0.246	0.81–0.91	0.59–0.47[c]
k_z dry (W/m K)	–	–	–	0.2
k_z char (W/m K)	0.1	0.062	1.25–1.6	0.15
k_z fib (W/m K)	–	–	–	0.1
C_p res (J/kg K)	1540	2500[b]	1100–1500	900–1470[c]
C_p dry (J/kg K)	–	–	–	1330
C_p char (J/kg K)	1300	1589[b]	1250–1600	1150
C_p fib (J/kg K)	–	794	–	794
h_{conv} (W/cm^2 K)	–	–	–	1.5×10^{-4}
ε_{res}	–	1	–	0.93
ε_{dry}	–	1	–	0.93
ε_{char}	–	1	–	0.86
ε_{fib}	–	1	–	0.792–0.06 (T/1000 K)
α_{res}	–	–	–	0.93
α_{dry}	–	–	–	0.93
α_{char}	–	–	–	0.98
α_{fib}	–	–	–	0.882–0.06 (T/1000 K)
Cp_{gas} (J/kg K)	–	0.72×10^3	9.63×10^3	2.0×10^3
α_c	–	–	–	0.55–1

[a] Fiberglass/epoxy.
[b] Properties reported for isolated components, not resin phase and fiber in composite.
[c] Temperature dependent [29].
[d] Phenol resin with glass filler (random orientation).

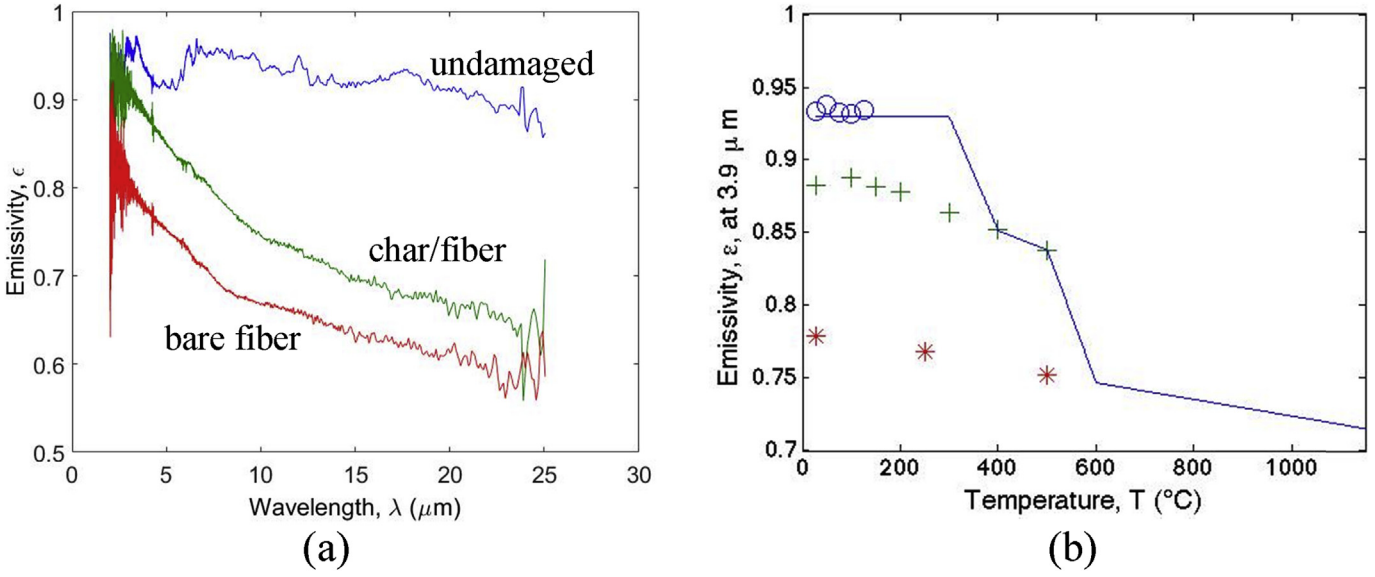

Fig. 9. Emissivity (a) decreases with wavelength and as decomposition progresses from [—] virgin resin to [—] char to [—] bare fiber at T = 750 C, and (b) emissivity at 3.9 μm decreases slowly as temperature increases.

4. Discussion

4.1. Thermal model

Descriptions of the thermal response of composite materials typically build on the Henderson model, which includes the effect of conduction, volatile convection, and enthalpy of decomposition [11,24]. Kinetics are represented by nth order Arrhenius reactions with one or more steps. Boundary conditions generally account for convection and radiation. Input material properties are usually phase specific with varying degrees of attention paid to temperature dependence. Extensions to the Henderson model are made in efforts to model additional effects including material expansion, volatile combustion, and damage due to internal gas pressure [25–27]. Temperature measurements are typically limited to thermocouple measurements at a small number of locations with typical response times of several seconds.

A three-dimensional, explicit, finite difference, thermal model

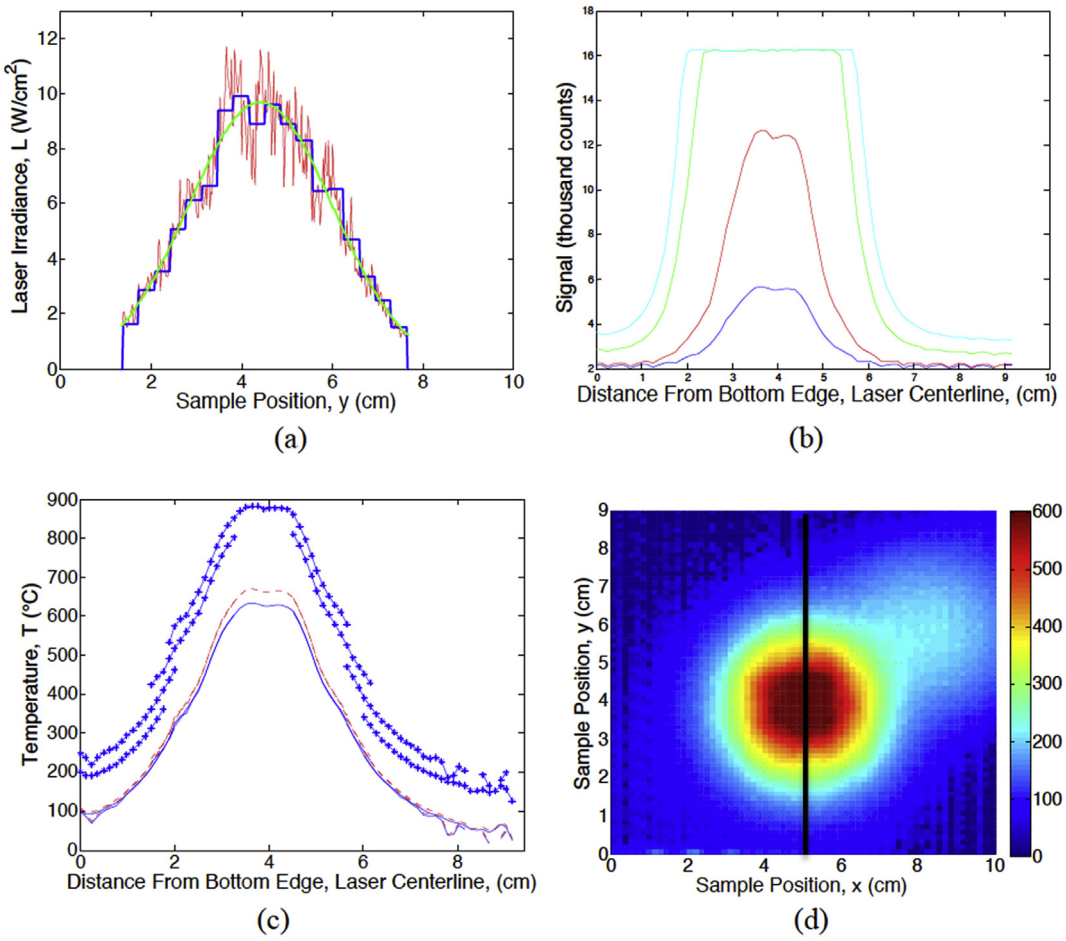

Fig. 10. (a) Instantaneous (□), temporally averaged (□) and modeled (□) laser irradiance profile in vertical direction at 9.9 W/cm^2 (b) uncalibrated signal at 4 integration times (0.1, 0.3, 2, and 4 ms) for a vertical slice through laser center, (c) calibrated temperatures ($\varepsilon = 1$) with varying offsets to illustrate overlap from different integration times (dotted lines), and $\varepsilon = 0.85$ (dashed line) with all integration times overlaid and (d) front side temperature map at 10 W/cm^2 and 30 s with temperature scale ranging from 0 to 600 °C.

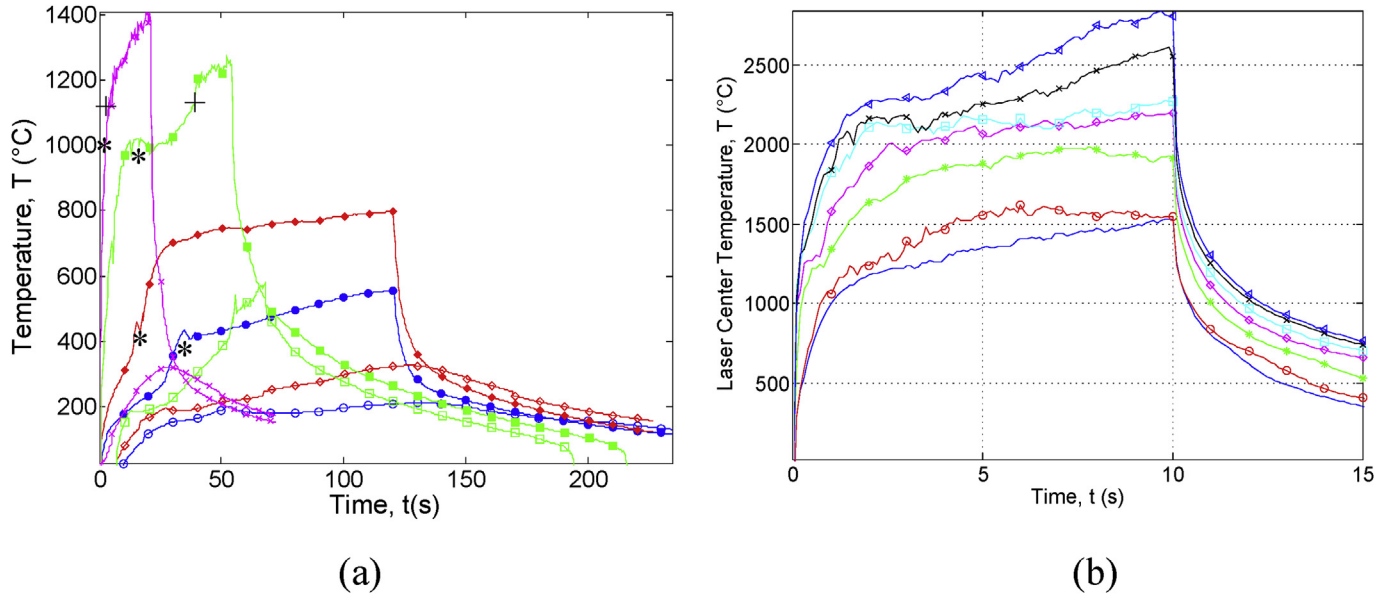

Fig. 11. (a) Front (filled symbols) and backside (open symbols) temperatures for a 3.2 mm thick panel at (●) 5 W/cm^2, (♦) 9.8 W/cm^2, (■) 35.7 W/cm^2, and (*) 63.7 W/cm^2 and (b) 2.5 cm × 15.2 cm x 0.32 cm thick (1.65 cm laser spot radius) strip laser center temperatures at 100 W/cm^2 (—), 152 W/cm^2 (○), 205 W/cm^2 (*), 296 W/cm^2 (◇), 396 W/cm^2 (□), 450 W/cm^2 (×), 520 W/cm^2 (△). Markers are included at point of maximum decomposition (*) and ignition (+).

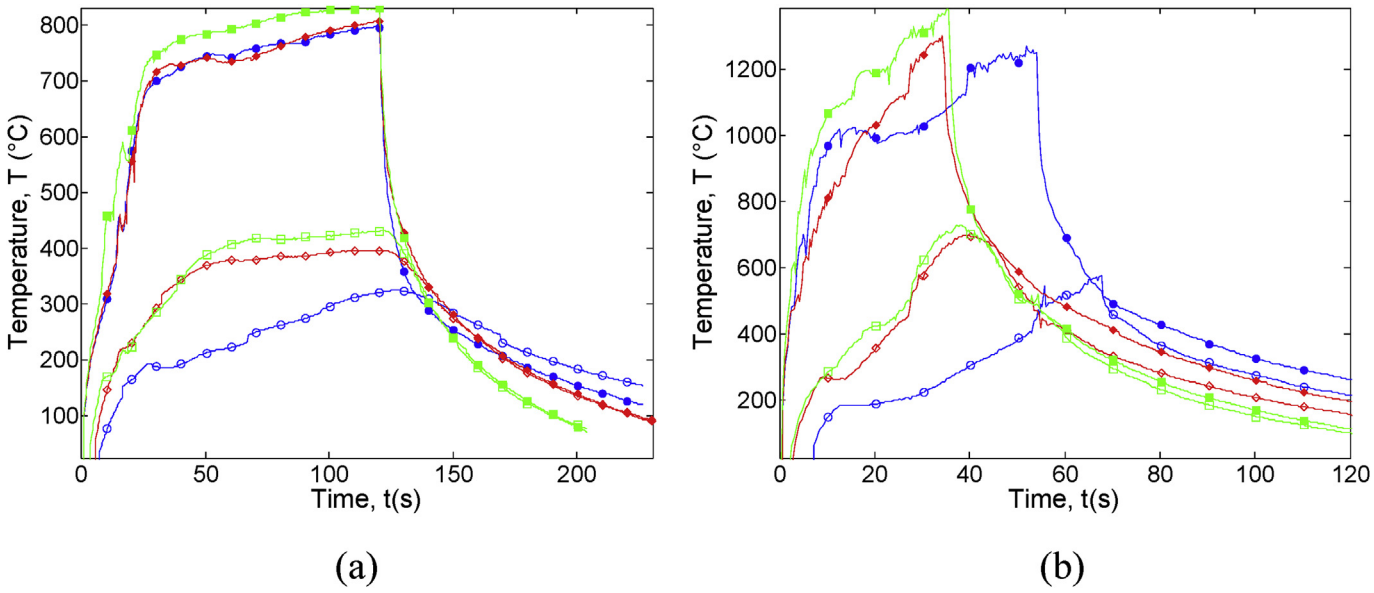

Fig. 12. Evolving temperatures at laser center for (a) 9.9 W/cm^2 and (b) 35.6 W/cm^2. Comparisons are made between (filled symbols) front surface and (open symbols) back surface laser center temperatures for sample thicknesses of (●) 3.2 mm (♦) 2.4 mm, and (■) 1.7 mm.

based on the heat diffusion equation was used in this work to estimate CFRP thermal properties and decomposition kinetics throughout matrix decomposition. Additional reaction source/sink terms for the heat of decomposition reactions and the convective flow of decomposition volatiles were included:

$$\rho C_p \frac{\partial T}{\partial t} = k_x \frac{\partial^2 T}{\partial x^2} + k_y \frac{\partial^2 T}{\partial y^2} + k_z \frac{\partial^2 T}{\partial z^2} + \sum \frac{Q_{rxn}}{V} \frac{dm_{rxn}}{dt} + \frac{Cp_{p,gas} \partial T}{V} \frac{dm_f}{dt} \quad (3)$$

as well as boundary conditions for convection, surface emission, and laser absorption:

$$k \frac{\partial T}{\partial x, y, z} = -h(T - T_\infty) - \varepsilon\sigma\left(T^4 - T_\infty^4\right) + \alpha L \quad (4)$$

where ρ, C_p, k, ε, α, and T are the composite density, specific heat, thermal conductivity, emissivity, absorptivity, and temperature of each element and h, σ, and T_∞ are the convection coefficient, Stefan-Boltzmann constant and ambient temperature. The reactions rates, dm_r/dt, mass flow rates, dm_f/dt and heat release, Q_r are developed further below. The surface absorption, α, and incident laser irradiance, $L = IA$, drive the material response.

The model mesh was 30×30 uniform elements in the plain perpendicular to the incoming laser, with an element for each carbon fiber ply in the parallel direction (8, 6, and 4 elements for 3.2, 2.4, and 1.7-mm thick samples, respectively). Computational stability was maintained by continually updating the time step according to the Courant-Friedrichs-Levy (CFL) condition [28]:

$$dt \leq \frac{\rho C_p \Delta}{2k_{max}} \quad \Delta = \frac{dx^2 dy^2 dz^2}{dx^2 dy^2 + dy^2 dz^2 + dx^2 dz^2} \quad (5)$$

as material properties changed with decomposition. Time steps generally ranged from 50 to 150 ms.

Conductivity (k) for CFRP is anisotropic, with higher conductivity along the fiber direction. The 2×2 twill weave of the samples provided equal conductivity in the plane perpendicular to the incoming laser (x and y directions). The conductivity in the thickness direction, k_z, parallel to the incoming laser, is much less due to the much lower conductivity of the resin matrix between plies. Material properties were assumed to change as the polymer matrix decomposition progressed, with the current properties in proportion to the relative amounts of each decomposition phase (virgin resin, dehydrated resin, char, and bare fiber) present in each cell. The fibers were assumed to be inert at these temperatures and exposure times. The heat capacity, $C_p(T)$ J/g K, and thickness conductivity, k_z W/m K, of the virgin CFRP material were measured by Kalogiannakis et al. using a modulated-temperature differential scanning calorimetric technique [29]:

$$C_p(T) = \begin{cases} 3.692\,x\,10^{-3}T + 0.8043 & T < 77.7\,^oC \\ 9.761\,x\,10^{-3}T + 0.3567 & 77.7\,^oC < T < 110.5\,^oC \\ 1.858\,x\,10^{-3}T + 1.1720 & T > 110.5\,^oC \end{cases} \quad (6)$$

$$k(T) = \begin{cases} 7.57\,x\,10^{-4}T + 0.56835 & T < 73\,^oC \\ -2.69\,x\,10^{-3}T + 0.8291 & 73\,^oC < T < 99\,^oC \\ 1.23\,x\,10^{-3}T + 0.4402 & T > 99\,^oC \end{cases} \quad (7)$$

where all temperatures are evaluated in °C. A different region (before, during, and after glass transition) is described for each property. The after-glass-transition equation was used to extrapolate values for temperatures beyond those reported, until the resin begins to decompose at 350 °C. Resin, char, and fiber densities were derived from literature [27] and supplier values and were used with measured sample densities to estimate sample fiber fraction.

The incident laser intensity distribution was measured throughout each experiment and combined into an average irradiance map as illustrated in Fig. 4(a). The scatter plate image resolution was reduced to match the front surface model mesh and assumed to be absorbed completely by the first few layers of carbon fibers of the topmost ply in accordance with high fiber absorption and scattering models [10]. Surface absorptivities at 1.07 μm of undamaged material, char, and bare fiber were measured with a spectrophotometer at room temperature and are reported in Table 1. The observations agree with prior measurements and

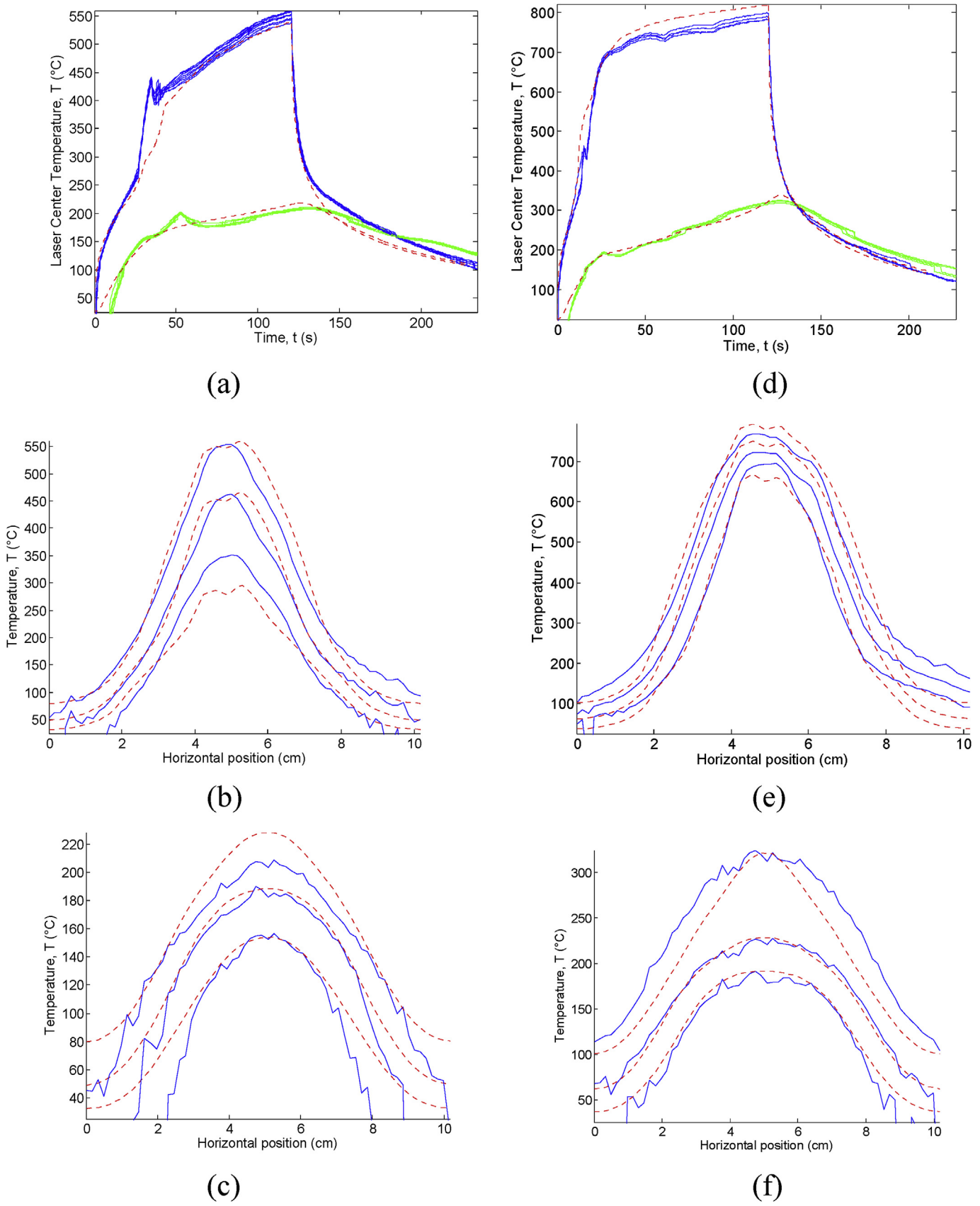

Fig. 13. Front (——), backside (——), and modeled (- - -) laser center temperatures of 3.2 mm thick panels at (a–c) 5 W/cm^2 and (d–f) 10 W/cm^2. Radial temperature profile comparisons are shown at 30, 60, and 120 s (increasing throughout).

simulations [10,30], and are assumed to be temperature independent for undamaged and charred material. It was assumed that the absorptivity of the bare carbon fibers began at the room temperature value measured with a spectrophotometer and decreased at the same rate as the fiber emissivity with increasing temperature. The measured room temperature absorptivities at 1.07 μm into the surface layer seem adequate for lower irradiance tests. However, as irradiance increases, large amounts of volatiles and soot are produced at the surface, absorbing and scattering the incoming beam to an unknown extent. This effect is estimated by modifying the absorptivity by an additional constant (α_c). At 35 and 64 W/cm^2, values for this constant of approximately 0.7 and 0.55, respectively, produce observed laser-center heating rates.

The Stefan-Boltzmann law, modified by the same temperature and phase-dependent surface emissivity curve used to determine the surface temperatures, is used to model surface emission losses. This approximation simplifies the model and introduces <5% error in radiated power at these temperatures compared to radiation loss calculated using measured spectral emissivity. Convection loss is approximated using calculated surface temperatures, ambient room temperature and a convective heat transfer coefficient calculated from natural convection from a vertical plate with average surface temperatures ($h = 1.5 \times 10^{-4}$ W/cm^2 K) [31]. Both radiation and convection are minor heat loss mechanisms at these temperatures.

Epoxy decomposition progresses sequentially from cured resin (k_{res}) to dehydrated resin (k_{dry}) to char with full char oxidation (k_{char}) to leave bare carbon fiber [32–36]:

$$resin \xrightarrow{k_{res}} dehydrated\ resin + H_2O \xrightarrow{k_{dry}} char + volatiles \xrightarrow{k_{char}} bare\ fiber + H_2O + CO_2 + soot \quad (8)$$

Resin decomposition kinetics were assumed to be first-order Arrhenius reactions:

$$\frac{dm_{res}}{dt} = -A_{res} m_{res} e^{-E_{res}/RT} \quad (9)$$

$$\frac{dm_{dry}}{dt} = r_{dry} A_{res} m_{res} e^{-E_{res}/RT} - A_{dry} m_{dry} e^{-E_{dry}/RT} \quad (10)$$

$$\frac{dm_{char}}{dt} = r_{char} A_{dry} m_{dry} e^{-E_{dry}/RT} - A_{char} m_{char} e^{-E_{char}/RT} \quad (11)$$

where A_{res}, A_{dry}, A_{char}, E_{res}, E_{dry}, and E_{char} are the Arrhenius pre-exponential factors and activation energies for epoxy resin, dehydrated resin, and char decomposition. Branching ratios, r_{dry} and r_{char}, are used to account for associated mass loss due to dehydrated water and volatile products produced during decomposition. Fibers were assumed to be inert at these relatively low-temperature, short-term exposures, having a sublimation temperature of approximately 3825 °C [37]. Energy produced or consumed by the dehydration, char-forming decomposition, and char-oxidizing reactions is assumed to be proportional to the mass undergoing the reaction [27] per time step as calculated in Eqs. (9)–(11) and added to the model as a source/sink term as shown in the fourth term in Eq. (3).

$$\sum \frac{Q_{rxn}}{V} \frac{dm_{rxn}}{dt} = Q_{p,res} \frac{dm_{res}}{Vdt} + Q_{p,dry} \frac{dm_{dry}}{Vdt} + Q_{p,char} \frac{dm_{char}}{Vdt} \quad (12)$$

This simplified approach is in line with prior kinetic studies [32,33] and mass loss modeling [35] of epoxy decomposition. Kinetic parameters are estimated in this work from fitting the thermal model simulation to measured temperatures from the mid-IR imagery.

The heat capacity of the departing decomposition products produce a cooling effect as described by the last term in Eq. (3). Mass loss due to dehydration, decomposition and char oxidation occurs throughout the material and products are heated as they exit. Taking a back-to-front approach, it is assumed that each model element must heat up the mass produced in it and all previous elements (in a given time step) over the temperature difference between the lower and current element. In this model, it is assumed that all mass loss has a constant heat capacity and that all mass exits through the front (laser incident) face. The value for the heat capacity of the departing gas (Cp_{gas}) is assumed to be similar to literature values [24] and is listed in Table 1.

4.2. Estimated kinetic and thermal properties

Figs. 13 and 14 show comparisons between predicted and observed temperatures at laser center. Radial profile comparisons through laser center at 30, 60, and 120 s are also provided. One set of thermal properties and kinetic parameters (Tables 1 and 2) describe the behavior of CFRP under all irradiance levels currently studied.

Initial heating until the start of the dehydration phase of decomposition (approximately 150 °C) is described well by conduction using the temperature dependent conductivity and heat capacity measured by Kalogiannakis et al. [29]. The conversion from virgin resin to dehydrated resin is accompanied by a significant reduction in conductivity in the thickness direction, leading to an increased surface heating rate (best illustrated by the 5 W/cm^2 case). This quickly leads to the primary decomposition step in which many of the bonds in the resin chemical structure are broken, producing volatile decomposition fragments and char. Both the dehydration and decomposition reactions are endothermic [11] and play a primary role (in addition to reduced thickness conductivity) in reducing the backside temperature increase. Further energy is lost due to the heat capacity of the departing volatiles. Together this produces a larger temperature gradient between the front and back surfaces and provides a heat sink that provides a momentary backside cooling effect. Modeling CFRP without the endothermic reaction enthalpies or volatile heat capacity increases the final backside temps by 100 and 90 °C at 5-and 10-W/cm^2 laser powers, respectively. Once decomposition has completed, char remains and begins to oxidize, which more slowly increases surface temperatures further due to reduced material density and thickness conductivity resulting from material swelling and enlarging of voids within the material. Initial cooling after the laser is turned off is rapid and dominated by radiation losses.

Prior TGA studies conducted at lower heating rates (0.2–3.3 °C/s) indicate that decomposition kinetics can vary with heating rate [27,28,33–35]. For example, Kandare et al. find that the decomposition temperature of a fiberglass/epoxy composite increases from 368 °C to 430 °C when heating rate is increased from 10 to 200 °C/min and the degradation mechanism simplifies from two stages to one [40]. However, only one set of thermal properties and kinetic parameters (listed in Tables 1 and 2) is required to describe the behavior of CFRP under all irradiance levels studied in this work. Heating rates leading to decomposition varied widely (12–330 °C/s) over the irradiance levels studied here, but did not require different kinetic rates to model. The stages and kinetics of the thermal decomposition of epoxy resins are well studied at low heating rates (<50 °C/min) using Thermogravimetric Analysis (TGA) [32,33,38–40]. At these rates, TGA experiments indicate that decomposition kinetics exhibit a heating rate dependence. HELs

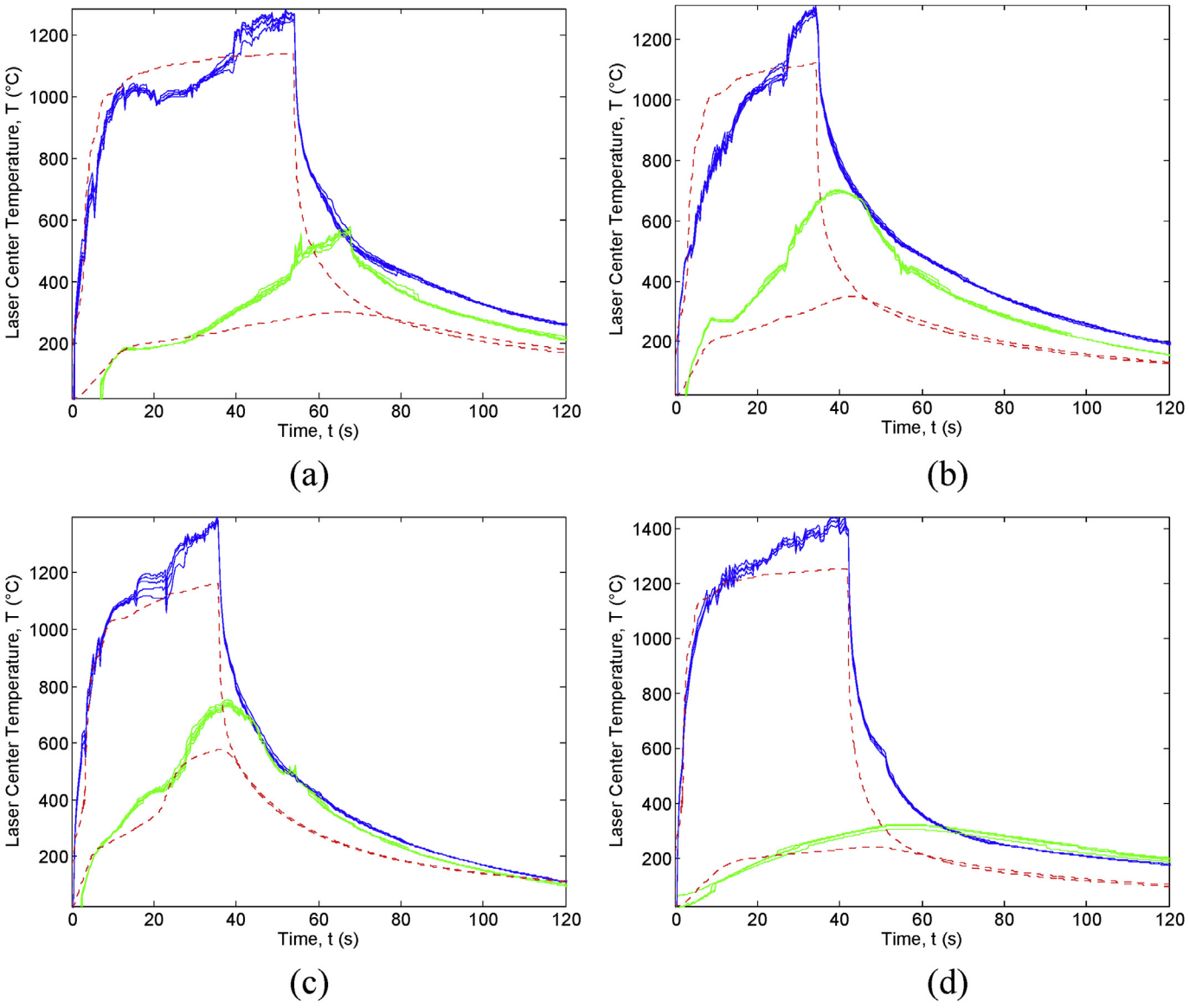

Fig. 14. Model fit (dashed) of front and back side temperatures at laser center. Multiple pixels near laser center are plotted for laser irradiances and sample thickness of: (a) 35.7 W/cm^2, 3.2 mm thick, (b) 35.7 W/cm^2, 2.4 mm thick, (c) 35.7 W/cm^2, 1.7 mm thick, (d) 63.7 W/cm^2, 3.2 mm thick.

Table 2
Kinetic parameters derived in this work compared with prior studies.

Parameter	[26]	[27]	[35]	[24]	This work
A_{res} (s^{-1})	–	–	3.6×10^8	–	1.8×10^8
Ea_{res} (kJ/mol)	–	–	125	–	89
A_{dry} (s^{-1})	2.16×10^6	3.15×10^{11}	8.1×10^4	1.98×10^{29} 8.16×10^{18}	9.7×10^9
r_{dry}	–	–	0.98	–	0.98
Ea_{dry} (kJ/mol)	117	182	92	260	120
n_{dry}	–	1.344	–	17.33 6.3	-
A_{char} (s^{-1})	–	–	1.1×10^5	2.61×10^7	1.8×10^8
r_{char}	0.53	–	–	–	0.4
Ea_{char} (kJ/mol)	–	–	120	354	150
n_{char}	–	–	–	0.53	
Q_p res (J/kg)	–	–	–	–	-1.3×10^6
Q_p dry (J/kg)	-0.198×10^6	-0.9×10^6	–	-0.234×10^6	-1.0×10^6
Q_p char (J/kg)	–	–	–	-2.093×10^6	0

produce very much higher heating rates (>500 °C/sec) that cannot be studied by TGA and yet may affect decomposition kinetics. It appears that the change responsible for the heating rate dependence saturated somewhere between the lower rates studied previously and the very high rates of the present study.

While the observations and model qualitatively agree for all conditions, several notable discrepancies exist. Fig. 13(a) shows a temperature spike during peak decomposition at 5 W/cm^2. However, decomposition is modeled as an endothermic process and so cools the sample. The spike may thus be due to thermal emission from the smoky plume. Plume emissivity is estimated to be approximately 0.015–0.03 at 3.9 μm for 5 W/cm^2 during the period of maximum surface decomposition using data collected with the imaging Fourier Transform Spectrometer. Using modeled and measured temperatures at the peak of decomposition, along with measured surface emissivity allows the estimation of the plume emissivity necessary to explain the observed effect. The necessary plume temperatures and emissivities range from $\varepsilon = 0.055–0.1$ at 3.9 μm and $T_{plume} = 1080–1300K$.

Another discrepancy exists in the backside temperatures of thinner samples at 9.9 W/cm^2. The model predicts gradual backside heating as the decomposition reactions proceed, leading to steady state temperatures at full backside char. Decomposition is incomplete with the thickest sample and completed quickly in the thinnest one, with good prediction. For medium thickness, the model predicts intermediate behavior, but the data is more reflective of the thinner samples.

The model developed here does not include gas phase combustion effects, which decreases the agreement in higher irradiance tests that achieve ignition, as shown in Fig. 14. Surface combustion is turbulent and produces an apparent surface heating of an additional 100–200 °C. As before, backside temperatures reach a quasi-steady state during dehydration and decomposition reactions (with a duration proportional to sample thickness), increasing after the reaction completes. In Fig. 14(a)-(c), the laser spot size fills almost the entire test panel, allowing the front surface flames to extend beyond the sample and ignite backside volatiles well before self-ignition. This leads to a similar increase in backside surface temperatures. In the case of Fig. 14(d), the laser spot size is reduced (2.3 cm), preventing premature backside ignition and the irradiance is higher, progressing rapidly through surface decomposition and decreasing thickness conductivity more rapidly. In all combustion cases, model temperatures during cool down are underestimated due to on-going combustion after the laser is turned off.

5. Conclusions

Front and backside emissivity-corrected temperature maps for the laser irradiation of CFRP at 1.07 μm and 5–64 W/cm^2 were observed and modeled to estimate resin decomposition kinetic parameters, the enthalpies of decomposition, and the thermal properties of decomposition reaction stages at high heating rates. Decomposition kinetics do not appear to be heating rate dependent at the high heating rates of 12–330 °C/s.

Ignition occurs at $T = 1198 \pm 50$ C independent of sample or irradiance. A laser irradiance threshold is observed near 21 W/cm^2, an order of magnitude higher than typically required for piloted ignition. Ignition of the back surface can occur at much lower temperatures (~700 C) when ignited by front surface combustion. The inverse of the ignition time is not linearly dependent on laser irradiance, as would be expected for the fixed ignition temperature. Resin mass is removed at a rate 109 mg/kJ without ignition and increases to 224 mg/kJ for ignition in a 2.3 cm spot. Irradiances of 5–64 W/cm^2 produced steady-state surface temperatures of 500–1300 °C, initial heating rates of 10–330 °C/s, and final backside temperatures of 180–450 °C. Increased heating rates are observed during decomposition (dehydration) with gradual heating at longer irradiation times. As sample thickness decreases from 3.2 to 1.7 mm, front side steady state temperatures increase by 190 °C. Front side cooling is more rapid than the backside, particularly for the thicker samples.

A thermal model with a single set of temperature dependent thermal, optical and kinetic parameters is reported and is sufficient to describe the evolving, spatially dependent, front and back surface temperature maps. Epoxy decomposition progresses sequentially from cured resin to dehydrated resin, to char with full char oxidation leaving bare carbon fiber. Fibers are inert at these relatively low-temperature, short-term exposures. Heat transfer is dominated by anisotropic conductivity, with higher conductivity along the fiber direction. The conversion from virgin resin to dehydrated resin is accompanied by a significant reduction in conductivity in the thickness direction, leading to an increased surface heating rate. Surface emissivity decreases with wavelength and temperature, as decomposition progresses. Both the dehydration and decomposition reactions are endothermic, reducing the backside temperature. Initial cooling after the laser is turned off is rapid and dominated by radiation losses.

While the observations and model qualitatively agree for all conditions, several limitations are noted. Thermal emission from the smoky plume and gas phase combustion effects are not included, which decreases the agreement for higher irradiance tests. In all combustion cases, model temperatures during cool down are underestimated due to continued combustion. Results are most sensitive to absorptivity, emissivity, heats of reactions, and conductivity of virgin resin, dehydrated resin, char, and bare carbon fiber as CFRP undergoes thermal decomposition. Knowing these parameters allows complex phenomenology of laser-material interactions to be adequately modeled with reduced dimensionality, yielding rapid progress on characterizing laser lethality.

Resin matrix removal from CFRPs as a result of HEL heating does not completely compromise the material, but does have detrimental effects including (1) the substantial production of decomposition products that can foul optics and electronics and provide a fuel source for combustion on both the exterior and interior of a CFRP panel and (2) severe reduction in the compressive strength of the CFRP. Material burn through is not necessary to severely damage the material as resin is completely removed at T = 450 °C at an energy deposited cost of approximately 9 kJ/g. Under buoyant conditions, epoxy decomposition of CFRP under high energy laser irradiation at 1.07 μm produces sufficient volatile decomposition products to support combustion at very low irradiances (<5 W/cm^2), but must have an ignition source or laser heated surface temperatures of 1198 ± 50 °C for ignition to occur. This finding is valid for laser spot sizes ranging from 1.65 to 6 cm diameter and laser powers from 5 to 525 W/cm^2.

Declarations of interest

None.

Acknowledgements

This work was supported in part by a grant from the High Energy Laser Joint Technology Office. The authors greatly appreciate the access to and support from the high power fiber laser facilities at the Air Force Research Laboratory, Directed Energy Directorate, Kirtland Air Force Base, New Mexico.

References

[1] C. Soutis, Fibre reinforced composites in aircraft construction, Prog. Aero. Sci. 41 (2005) 143–151, https://doi.org/10.1016/j.paerosci.2005.02.004.

[2] L.A. Burns, S. Feih, A.P. Mouritz, Compression failure of carbon fiber-epoxy laminates in fire, J. Aircraft 47 (2010) 528–533, https://doi.org/10.2514/1.45065.

[3] S. Feih, A.P. Mouritz, Composites : Part A Tensile properties of carbon fibres and carbon fibre – polymer composites in fire, Compos. Part A 43 (2012) 765–772, https://doi.org/10.1016/j.compositesa.2011.06.016.

[4] A.Y. Snegirev, V.A. Talalov, V.V. Stepanov, J.N. Harris, A new model to predict pyrolysis, ignition and burning of flammable materials in fire tests, Fire Saf. J. 59 (2013) 132–150. https://doi.org.wrs.idm.oclc.org/10.1016/j.firesaf.2013.03.012.

[5] A.G. Gibson, A.P. Mouritz, Y. Wu, C.P. Gardiner, Z. Mathys, Validation of the Gibson Model for the Fire Reaction Properties of Fibre-polymer Composites, Newcastle, 2003.

[6] G.P. Perram, S.J. Cusumano, R.L. Hengehold, S.T. Fiorino, An Introduction to Laser Weapons Systems, Directed Energy Professional Society, 2010.

[7] R.J. Bartell, G.P. Perram, S.T. Fiorino, S.N. Long, M.J. Houle, C.A. Rice, et al., Methodology for comparing worldwide performance of diverse weight-constrained high energy laser systems, Proc. SPIE 5792 (2005) 76–87, https://doi.org/10.1117/12.603384.

[8] V.C. Coffey, High energy lasers: new advances in defense applications, Optic Photon. News 25 (10) (2014) 28–35.

[9] T. Stratoudaki, C. Edwards, S. Dixon, S.B. Palmer, Optical absorption of epoxy resin and its role in the laser ultrasonic generation mechanism in composite materials, Rev. Quant. Nondestruct. Eval 22 (2003) 965–972.

[10] C.D. Boley, A.M. Rubenchik, Modeling of laser interactions with composite materials, Appl. Opt 52 (2013) 3329–3337.

[11] A.P. Mouritz, A.G. Gibson, Fire Properties of Polymer Composite Materials, first ed., Springer, Dordrecht, 2006.

[12] J.L. Massman, K.C. Gross, Understanding the influence of turbulence in imaging Fourier transform spectroscopy of smokestack plumes, Proc. SPIE. 8048 (n.d.) 80480A. doi:- 10.1117/12.883197 [doi].

[13] E.A. Moore, K.C. Gross, S.J. Bowen, G.P. Perram, M. Chamberland, V. Farley, et al., Characterizing and overcoming spectral artifacts in imaging Fourier-transform spectroscopy of turbulent exhaust plumes, Proc. SPIE. 7304 (n.d.) 730416. doi:- 10.1117/12.818710 [doi].

[14] K.C. Bradley, K.C. Gross, G.P. Perram, Imaging Fourier Transform Spectrometry of Chemical Plumes, Proc. SPIE. 7304 (n.d.) 73040J. doi:- 10.1117/12.816711 [doi].

[15] S. Savary, J.-P. Gagnon, K. Gross, P. Tremblay, M. Chamberland, V. Farley, Standoff identification and quantification of flare emissions using infrared hyperspectral imaging, Proc. SPIE. 8024 (n.d.) 80240T. doi:- 10.1117/12.884342 [doi].

[16] R.I. Acosta, K.C. Gross, G.P. Perram, S.M. Johnson, L. Dao, D.F. Medina, et al., Gas-phase plume from laser-irradiated fiberglass- Reinforced polymers via imaging fourier transform spectroscopy, Appl. Spectrosc. 68 (2015) 723–732, https://doi.org/10.1366/13-07213.

[17] R.I. Acosta, K.C. Gross, G.P. Perram, Thermal degradation of Poly(methyl methacrylate) with a 1.064 μm Nd:YAG laser in a buoyant flow, Polym. Degrad. Stabil. 121 (2015) 78–89, https://doi.org/10.1016/j.polymdegradstab.2015.06.016.

[18] R.I. Acosta, K.C. Gross, G.P. Perram, Combustion kinetics of laser irradiated porous graphite from imaging Fourier transform spectroscopy, Combust. Flame 163 (2015) 90–99, https://doi.org/10.1016/j.combustflame.2015.09.004.

[19] S.M. Baumann, C. Keenan, M.A. Marciniak, G.P. Perram, Spectral and temperature-dependent infrared emissivity measurements of painted metals for improved temperature estimation during laser damage testing, Proc. SPIE 9237 (2014) 923713, https://doi.org/10.1117/12.2068435.

[20] K.N.C. Gross, K.C. Bradley, G.P. Perram, Remote identification and quantification of industrial smokestack effluents via imaging fourier-transform spectroscopy, Environ. Sci. Technol. 44 (2010) 9390–9397, https://doi.org/10.1021/es101823z.

[21] N. Grassie, M.I. Guy, N.H. Tennent, Degradation of epoxy Polymers : Part 4 thermal degradation of bisphenol-a diglycidyl ether cured with ethylene diamine, Polym. Degrad. Stabil. 14 (1986) 125–137.

[22] S.M. Baumann, B.E. Hurst, M.A. Marciniak, G.P. Perram, Fiber laser heating and penetration of aluminum in shear flow, Opt. Eng. 53 (2014) 122510, https://doi.org/10.1117/1.OE.53.12.122510.

[23] N.C. Herr, Degradation of Carbon Fiber Reinforced Polymer and Graphite by Laser Heating, Air Force Institute of Technology, 2016.

[24] J.B. Henderson, J.A. Wiebelt, M.R. Tant, A model for the thermal response of polymer composite materials with experimental verification, J. Compos. Mater. 19 (1985) 579–595.

[25] J.B. Henderson, T.E. Wiecek, A mathematical model to predict the thermal response of decomposing, expanding polymer composites, J. Compos. Mater. 21 (1987) 373–393.

[26] E.D. McCarthy, B.K. Kandola, G. Edwards, P. Myler, J. Yuan, Y.C. Wang, et al., Modelling flaming combustion in glass fibre-reinforced composite laminates, J. Compos. Mater. 47 (2012) 2371–2384, https://doi.org/10.1177/0021998312457962.

[27] R.D. Chippendale, I.O. Golosnoy, P.L. Lewin, Numerical modelling of thermal decomposition processes and associated damage in carbon fibre composites, J. Phys. D Appl. Phys. 47 (2014) 385301, https://doi.org/10.1088/0022-3727/47/38/385301.

[28] E. Gutierrez-Miravete, Chapter 6 Numerical Methods for Transient Problems, (n.d.) 1–22. http://www.ewp.rpi.edu/hartford/~wallj2/CHT/Notes/ch06.pdf (accessed March 16, 2016).

[29] G. Kalogiannakis, D. Van Hemelrijck, G. Van Assche, Measurements of thermal properties of carbon/epoxy and glass/epoxy using modulated temperature differential scanning calorimetry, J. Compos. Mater. 38 (2004) 163–175, https://doi.org/10.1177/0021998304038647.

[30] R.K. Freeman, F.A. Rigby, N. Morley, Temperature-dependent reflectance of plated metals and composite materials under laser irradiation, J. Thermophys. Heat Tran. 14 (2000) 305–312, https://doi.org/10.2514/2.6546.

[31] F.P. Incropera, D.P. DeWitt, Fundamentals of Heat and Mass Transfer, fourth ed., John Wiley & Sons, Ltd., New York, 1996.

[32] N. Rose, M. Le Bras, S. Bourbigot, R. Delobepb, B. Castes, Comprehensive study of the oxidative degradation of an epoxy resin using the degradation front model, Polym. Degrad. Stabil. 54 (1996) 355–360.

[33] N. Rose, M. Le Bras, S. Bourbigot, R. Delobel, Thermal oxidative degradation of epoxy resins : evaluation of their heat resistance using invariant kinetic parameters, Polym. Degrad. Stabil. 45 (1994) 387–397.

[34] E. Kandare, B.K. Kandola, D. Mccarthy, P. Myler, G. Edwards, Y. Jifeng, et al., Fiber-reinforced epoxy composites exposed to high temperature environments. Part II : modeling mechanical property degradation, J. Compos. Mater. 45 (2010) 1511–1521, https://doi.org/10.1177/0021998310385024.

[35] E. Kandare, B.K. Kandola, J.E.J. Staggs, Global kinetics of thermal degradation of flame-retarded epoxy resin formulations, Polym. Degrad. Stabil. 92 (2007) 1778–1787, https://doi.org/10.1016/j.polymdegradstab.2007.07.011.

[36] N. Rose, M. Le Bras, R. Delobel, B. Costes, Y. Henry, Thermal oxidative degradation of an epoxy resin, Polym. Degrad. Stabil. 42 (1993) 307–316.

[37] P. Mucha, R. Weber, N. Speker, P. Berger, B. Sommer, T. Graf, Calibrated heat flow model for determining the heat conduction losses in laser cutting of CFRP, Phys. Procedia 56 (2014) 1208–1217, https://doi.org/10.1016/j.phpro.2014.08.036.

[38] K.S. Chen, R.Z. Yeh, Pyrolysis kinetics of epoxy resin in a nitrogen atmosphere, J. Hazard Mater. 49 (1996) 105–113.

[39] P. Budrugeac, E. Segal, Application of isoconversional and multivariate non-linear regression methods for evaluation of the degradation mechanism and kinetic parameters of an epoxy resin, Polym. Degrad. Stabil. 93 (2008) 1073–1080, https://doi.org/10.1016/j.polymdegradstab.2008.03.017.

[40] E. Kandare, B.K. Kandola, P. Myler, G. Edwards, Thermo-mechanical responses of fiber-reinforced epoxy composites exposed to high temperature environments. Part I: experimental data acquisition, J. Compos. Mater. 44 (2010) 3093–3114, https://doi.org/10.1177/0021998310373511.